Energy 276 (2023) 127507

Contents lists available at ScienceDirect

Energy

journal homepage: www.elsevier.com/locate/energy

Dynamics and products of potato crop residue conversion under a pyrolytic runaway regime - Influences of feedstock variability

Carmen Branca [a], Antonio Galgano [b], Colomba Di Blasi [b,*]

[a] Istituto di Scienze e Tecnologie per l'Energia e la Mobilità Sostenibili (STEMS), C.N.R.,P. le V, Tecchio, 80125, Napoli, Italy
[b] Dipartimento di Ingegneria Chimica, dei Materiali e della Produzione Industriale, Università degli Studi di Napoli "Federico II", P. le V, Tecchio, 80125, Napoli, Italy

ARTICLE INFO

Handling Editor: Krzysztof (K.J.) Ptasinski

Keywords:
Pyrolytic runaway
Potato crop residues
Overheating
Residue variability
Char structure

ABSTRACT

Potato, ranked third among food crops, gives rise to huge amounts of plant residues largely unutilized owing to the presence of toxic compounds. The fundamentals of the pyrolytic runaway of these residues are investigated for a packed bed heated at a temperature of 570 K. The feedstock variability (five samples of different harvest year and cultivar), corresponding to variable average plant ageing, causes remarkable differences in the characteristic times (values between 6 and 42 s), heating rates (maxima between 5 and 155 K/s) and temperature overshoots (maxima between 220 and 410 K) of the runaway. On the other hand, the total gas and char yields are approximately the same (60–63 wt%), in consequence of the always fast and severe self-heating, also leading to evenly distributed and intense melting phenomena. The very high potassium contents (about 5–8 wt%) and a cellular structure with low porosity are the chief properties responsible for the significant exothermicity, resulting in intrinsically fast, in-situ catalyzed pyrolysis. The enhancement in the thermal severity of the pyrolytic runaway with longer plant ageing can be attributed to higher cellulose/starch contents, producing larger amounts of more reactive vapors, and thicker stem walls, confirming the key role of secondary reactions for the process.

1. Introduction

Though the importance of pyrolysis for the complete transformation of biomass into useful products is widely acknowledged, a recent review [1] provides evidence that both technological and economic factors impede its commercial-scale development. For instance, for fixed bed reactors generally applied for waste conversion [2], scale-up becomes complicated because volumetric feed heating is achieved via an external heat supply through a surface. Hence the effectiveness of the external heat transfer to the bed may drastically change with the scale of the process. This consequently impacts on the product properties and the cost for the external heating equipment. In this regard, the biomass gasification concepts [3] are also introduced for pyrolysis. They consist of two main approaches, defined by the modality heat is provided to the gasifier. For the autothermal conversion, heat is provided by partial combustion of the feed/products. For the allothermal case, heat is supplied by an external source. Self-sustained pyrolysis, based on the combustion of the gas product [4,5], or oxidative pyrolysis[6–9] (versus the usual pyrolysis carried out under inert atmosphere) are also proposed. However, experimental evidence exists that biomass pyrolysis can give rise to significant exothermicity [10].

The exothermicity of lignocellulosic material pyrolysis is clearly shown by packed beds or particles [11–18] exposed to uniform and fast heating along the lateral surfaces. However, the exothermicity magnitude is anyway important for all the reactor configurations [10], contributing to reduce the heat requirements. Moreover, a surprising new conversion regime, named pyrolytic runaway [19–21], has been identified for packed-bed pyrolysis. The main feature is the extremely rapid and highly exothermic conversion of the entire feed after a much longer pre-heating period. It should be stressed that the thermal conditions during conversion are determined by self-heating and are highly different from those externally imposed. This leads to changes in the product yields and composition [22]. Moreover, given the short time scales of runaway conversion, the quality of the feedback control may also deteriorate. Yet the volumetric heat generation from the pyrolysis reactions, properly controlled, could be adequately exploited to bring the feed first to the activation temperature and then to guarantee complete conversion [23]. This would ultimately lead to a nearly autothermal process without the complications introduced by the presence of oxygen.

A precise comprehension of the feedstock properties that allow for

* Corresponding author.
E-mail address: diblasi@unina.it (C. Di Blasi).

https://doi.org/10.1016/j.energy.2023.127507
Received 28 November 2022; Received in revised form 8 April 2023; Accepted 10 April 2023
Available online 13 April 2023

Nomenclature

Pyrolytic runaway

$dt_{overh} = t_d - t_{pri}$ time interval for the overheating (s)
$dt_{pr} = t_{amax} - t_{pri}$ time interval for the pyrolytic runaway (s)
dY_G rate of gas release (the time derivative of the mass fraction of the gas released, referred to the initial sample mass) (1/s)
dY_{Gpeak} peak of the rate of gas release (1/s)
h_{ab} average bed heating rate (K/s)
h_b maximum local bed heating rate (K/s)
T temperature (K)
t time (s)
T_a spatially averaged temperature (K)
T_{ah} the spatially averaged temperature of the char bed, after complete conversion (K)
T_{aind} spatially averaged temperature of the bed at the induction time (K)
T_{amax} maximum of the spatially averaged temperature (K)
t_{amax} time when the maximum spatially average temperature is attained (s)
T_{aoverh} average temperature, over time and space, for the time interval dt_{overh} (K)
T_{apr} average temperature, over time and space, for the time interval dt_{pr} (K)
T_{apri} spatially averaged temperature of the bed at the beginning of the pyrolytic runaway (K)
t_d decay time (time corresponding to a reduction of 90% in the spatially averaged temperature overshoot) (s)
T_h heating temperature (the steady temperature of the char bed, after complete conversion, at a distance of 5 mm from the heat exposed surface) (K)
t_{ind} induction time (time when a local point/zone of the bed exhibits a sudden increase in the heating rate) (s)
T_{max} absolute maximum temperature (K)
t_{max} time when the maximum temperature is attained (s)
t_{pri} time when the pyrolytic runaway begins (it corresponds to a steep increase (2 K/s) in the time derivative of the spatially averaged temperature) (s)
Y_{Gind} percentage of gas released at the induction time
Y_{Gpri} percentage of gas released at the beginning of the pyrolytic runaway
ΔT_{max} maximum local temperature overshoot (difference between the maximum temperature and the steady final value at the same spatial position) (K)
ΔT_{amax} maximum averaged temperature overshoot, ((the difference between the maximum average temperature and the steady average value of char) (K)

Thermo-gravimetric and calorimetric parameters

$-dY/dt_{peak}$ peak rate of DTG curves (1/s)
fwhm temperature range corresponding to the full width of the DTG curve at the half maximum (K)
H_R global primary reaction heat (J/g)
T_{dec} temperature corresponding to the release of 50 wt% of the total volatiles from DTG curves (K)
T_{peak} temperature corresponding to the peak rate of DTG curves (K)
$Y_{V550-600}$ volatile mass fraction lost in the temperature range 550–600 K
Y_{773} solid mass fraction detected at 773 K from the thermogravimetric curves

this conversion regime is not yet achieved. Based on the results currently available, it appears that a positive item is the scarcely porous structure of some residues [19–21] which makes longer the intra-particle residence times of primary organic vapors, thus enhancing secondary exothermic reactions [24]. The impregnation of both basic [25–28] and acidic [29–31] catalysts in wood, favoring char formation, is another important factor. It is also understandable that the magnitude of pyrolytic runaway is dependent on the size of the particles [32] and the initial moisture level [33].

Among the feedstocks undergoing pyrolytic runaway, potato crop residues exhibited the highest exothermicity display [20] (temperature overshoots up to 300 K versus about 200 K for other lignocellulosic residues, such as fruit shells and stones [19,21]). The conversion times are only about 4–15% of the pre-heating times. These residues are available in huge amounts throughout the world as potato is the third quantitative most important food crop [34]. It is also an excellent candidate for advanced sustainable agri-food systems [35]. The presence of toxic glycol-alkaloids in all parts of the plant [36] and the treat of environmental pollution for field disposal are not adverse factors for waste transformation by pyrolysis. However, the specific features, responsible for the high exothermicity, were not investigated [20]. Also, it is not known whether the high pyrolysis exothermicity was peculiar of that specific sample or generally valid for this category of residues. In fact, it is acknowledged that biomass feedstocks (wood, energy crops and agricultural residues) [37–39] have inherent variability, originated from variety/genotype, environmental and production issues which affect their chemico-physical properties and consequently the conversion process.

The main scope of this study is to further investigate biomass conversion under the regime of pyrolytic runaway. Potato crop residues are again considered, with the scope of identifying the factors responsible for the high exothermicity previously observed. The effects of feedstock variability are also examined, using five samples of different variety and harvest year. After feedstock characterization, packed-bed pyrolysis is carried out, obtaining data about temperature dynamics and yields and composition of products, including the char morphological structure.

2. Materials and methods

Five samples of potato (Solanum tuberosum L.) crop residues are considered (samples N.1-5). They refer to three cultivars (Spunta, Désirée and Everest, all reported to be medium height plants), grown in two different zones (Table 1) of Irpinia (South Italy). Given the small area, the geographical origin is not expected to be important. The cultivation method is also the same while the harvest refers to the years 2016, 2017 and 2018. The main residue characteristics appear to depend on the stem height. This is essentially determined by the seasonality (for instance, frequent rain favors plant growth) and the required early or late harvest. The variability induced by these factors, at the harvest time, can be roughly described by variable plant ageing. It is understandable that, on the average, the ageing decreases from the late to the early harvest (or as the harvest time becomes shorter). For the same harvest time, it is shorter for the taller plants given that growth occurs as the stems (and roots) lengthen. Moreover, the stem walls are thinner for the less aged plants. Based on these considerations and the sample characteristics listed in Table 1, an ageing level is introduced as short (sample N.3), medium (samples N.4,5) and long (samples N.1,2). Snapshots of the entire residue (sample N. 5) and stems (samples N.2 and N.5) are shown in Fig. 1.

Residues are made mainly of stems amounting to about 80–85 wt% (the remaining part consists of branches and foliage), which determine the main characteristics of the thermochemical behavior (roots are

Table 1
Potato crop residue variability for the samples N.1-5, based on the cultivar, geographical area (comunità montana Alta Irpinia (cmAI) and comunità montana Terminio Cervialto (cmTM) of Irpinia (South Italy)), harvest year, stem height, harvest type (early harvest: 100 days after plantation; late harvest: 130 days after plantation), and average plant ageing level.

Sample Number	Cultivar	Geographical area	Harvest year	Stem height	Harvest type	Average ageing level
1	Spunta	cm AI	2016	40–50 cm	early	Long
2	Désirée	cm AI	2017	40–50 cm	late	Long
3	Everest	cm AI	2017	90–130 cm	early	Short
4	Spunta	cm TC	2017	70–90 cm	early	Medium-long
5	Spunta	cm AI	2018	80–110 cm	early	Medium-short

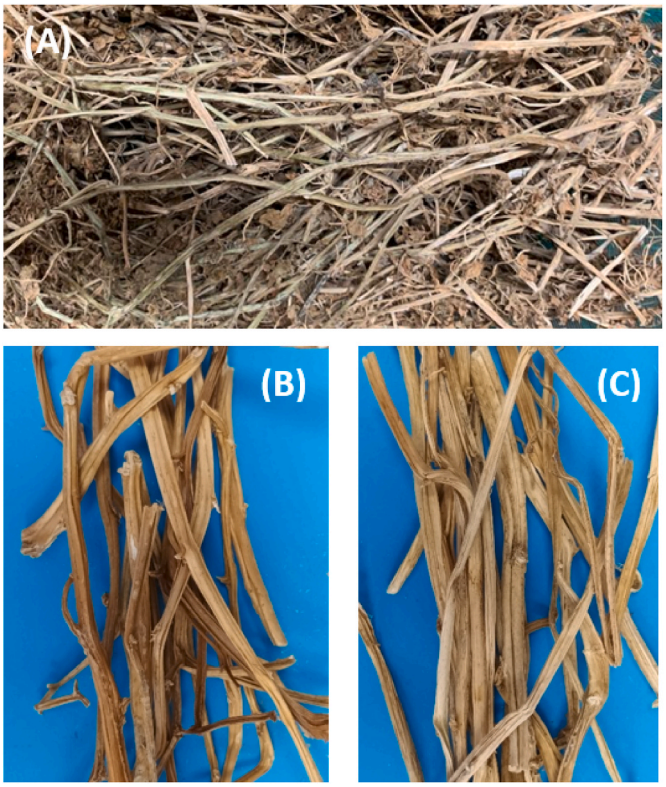

Fig. 1. Snapshots of the potato crop residues: entire plant (A, sample N.5), stems for the sample N.2 (B) and N.5 (C).

excluded from the analysis to avoid soil contamination). Preliminary tests indicate that foliage does not contribute significantly to the process exothermicity. Branches roughly behave as the top part of the stems. For these reasons, sample characterization is focused on the stems and includes the proximate analysis, carried out using thermogravimetry and the same procedure previously described [40], the ICP-MS analysis of the ashes, and the Scanning Electron Microscope (SEM) and Energy Dispersive X-ray (EDX) analysis of the morphological structure. A complete description of the thermogravimetric behavior and the decomposition kinetics of the samples N.1-5 is already available [41]. However, the main thermogravimetric parameters are also examined here (measurements made by a Mettler TGA 1 system, with a pulverized (particle sizes below 90 μm) sample mass of 2 mg, a heating rate of 5 K/min up to 773 K and a nitrogen flow of 50 mL/min). Differential Scanning Calorimetry (DSC, calorimeter Mettler DSC 1/700) measurements (and corresponding thermogravimetric curves) are also made. A sample mass of 5 mg is heated at 20 K/min up to 773 K, under a nitrogen flow of 160 mL/min, including a pre-drying stage at 383 K for 20 min, in aluminum open crucibles.

Details on the packed-bed pyrolysis are available in previous works [16,17,19–21] and presented in the attached Supplementary Material (SM) (reactor schematic in Fig. SM1). In brief, the pyrolysis experiments are conducted using a cylindrical packed bed (4 cm diameter and height) exposed along the lateral surface to a constant and uniform radiative heat flux (maximum heating rate of the heater around 750 K/s). The reactor, where the packed bed is allocated, is a quartz tube with a wider (6 cm) diameter. The inert reaction environment is achieved by means of a forced nitrogen flow. The temperature field is measured, at the median section of the bed, using 500-μm thermocouples. They are vertically arranged with careful manual adjustment of the particles to avoid possible flow channeling. The nitrogen stream, due to the resistance offered by the packed particles, mainly flows along the lateral surface of the bed. The temperature gradients along the vertical direction are expected to be negligible. Indeed, the relatively short bed is positioned in the isothermal zone of the heater, so that they may be caused only by the small variations in the convective heat exchange (nominal velocity 1.3 cm/s). During pyrolysis, convective transport is essentially determined by the release of high amounts of volatile products. This is an intrinsic characteristic of lignocellulosic materials. In any case, measurements along the radial direction, at the median section, provide meaningful information about the dynamics of the thermal field, as confirmed by sound correlations between this and the bed weight loss curves for both wood and agricultural residues [16,17,19] (also for wood cylinders of the same size as the packed bed [17]). After radiative heating, heat and mass transfer (conduction/diffusion and convection) across the bed takes place, interacting with primary and secondary reactions and related thermicity. At very high temperatures, caused by high external heat fluxes or high reaction exothermicity, intra-bed radiative heat transfer also becomes important.

The feedstock batches, to be used for the experiments, are carefully prepared for each of the samples N.1-5, to ensure uniform average properties (e. g. stem sizes, proportions and characteristics of the various parts of the plant). In all cases, the sample always consists of 80 and 20 wt% of stems and branches/foliage, respectively. This approach permits to obtain a good reproducibility of the measurements even when a pyrolytic regime is established [20] and to facilitate the comparison of various samples.

Stems are cut into about 5 mm sized pieces. For the given size of the packed bed, the initial sample mass, on a dry basis, is around 9 g (9.7 g for the sample N.3). In this way, the bulk density of the packed bed is approximately the same (maximum variation around 8%). Consequently, though not measured, the permeability to gas flow is also expected to remain roughly unvaried for the various samples. In all cases, oven drying overnight at 353 K, followed by 2 h at 373 K, is applied. The packed-bed experiments are made using an external radiant heat flux of 21.55 kW/m^2, corresponding to a heating temperature, T_h, around 570 K. The heating temperature is the steady value, after complete conversion, at 5 mm from the heat exposed surface [16]. It was observed [20] that, for the sample N.2, this external heat flux gives rise to a conversion regime of pyrolytic runaway, following an abrupt transition from torrefaction.

The information gained from the experiments concerns the thermal field (five thermocouples positioned at the median section of the bed starting from r = 0 (center) to 1.9 cm (subsurface), Fig. SM1 of the SM) and the yields of the lumped product classes together with the composition of the gas [42]. SEM-EDX analyses are applied to characterize the

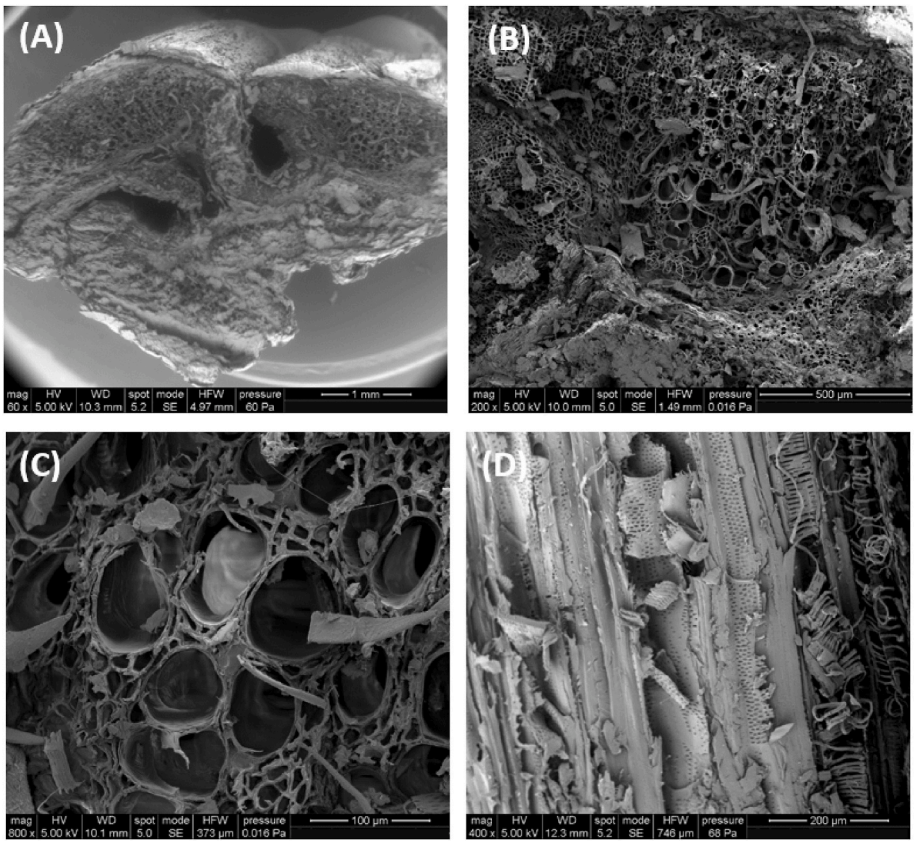

Fig. 2. A–D – SEM images of the potato plant stem for the cross section (A) and details of the structure for the cross (B, C) and longitudinal (D) stem directions (sample N.2).

morphological structure of chars. The composition of the liquid product is also analyzed, using GC-MS and the conditions previously reported [42] and summarized in the SM.

3. Results and discussion

After the results of sample characterization, the main features of the pyrolytic runaway are presented for the samples N.1-5. The effects are discussed of the feedstock variability, in terms of characteristic temperatures and times. The yields of the three lumped product classes, with the composition of the gas and the liquid, are also examined. Finally, SEM-EDX analyses of chars are shown and commented.

3.1. Residue characterization - structure and proximate analysis

SEM images of the potato plant stem are shown in Fig. 2A–D for the sample N.2. Those of the other samples are qualitatively similar. A hollow structure appears with one, two (Fig. 2A) or more wide openings, essentially depending on the stem height (maximum stem diameters around 1–2 cm). The wall thickness varies from about 3 to 1 mm or less (from the bottom to the top part of the stem). Hence, on the average, it is smaller for the less aged samples. It is likely that the thinner particles of the sample N.3 give rise to a denser packing of the bed, resulting into a slightly higher initial mass for the pyrolysis experiments. As for the activity of secondary reactions, it should also be mentioned that the thickness of the stem wall is the characteristic size. In fact, for the pyrolytic runaway of hazelnut shells [32], it was found that, if the particles preserve the thickness structure, the process dynamics are not altered by size reduction. Instead, the magnitude of the exotherm is strongly reduced or almost disappear for milled samples, even in the pelletized form. In fact, to get powdered samples the particle thickness is destroyed. The same behavior is also reasonably expected from the potato crop residues.

The potato stem cross section shows a cellular network, with open or

Table 2
Proximate analysis and ICP-MS characterization of the ashes (alkali metals) of the potato crop residues (stems), samples N.1-5.

Sample Number	VM [% wt]	FC [% wt]	ASH [%wt]	K [ppm]	Ca [ppm]	Mg [ppm]	Na [ppm]
1	77.1	11.2	11.7	82930	10770	3864	323.1
2	76.9	12.6	10.5	58420	15590	3999	339
3	77.0	11.3	11.7	75030	12130	1613	174.8
4	76.4	14.0	9.6	50320	12200	323.6	242.2
5	79.0	11.4	9.6	73800	5768	1859	235.8

Table 3
Thermogravimetric parameters (heating rate 5 K/min) for the potato crop residues (stems), samples N.1-5: peak rates of mass loss, $-dY/dt_{peak}$, and corresponding temperatures, T_{peak}, temperature range corresponding to the full width of the rate curve at half maximum, fwhm, mass fraction at a temperature of 773 K, Y_{773}, decomposition temperature (corresponding to 50 wt% of mass loss), T_{dec}, and volatile mass fraction released in the temperature range 550–600 K, $Y_{V550\text{-}600}$, and global reaction heat, H_R.

	Sample Number				
	1	2	3	4	5
T_{peak} [K]	570	576	554	558	555
T_{dec} [K]	563	567	549	550	550
fwhm [K]	38	33	70	50	49
$-dY/dt_{peak}$ x 10^3 [s^{-1}]	0.71	0.70	0.53	0.66	0.64
Y_{773}	0.39	0.38	0.39	0.36	0.37
$Y_{V550-600K}$	0.28	0.27	0.17	0.23	0.24
H_R [Jg^{-1}]	−357	−324	−181	−248	−420

closed alveola of variable sizes closely interconnected (Fig. 2B-C). Long void channels (Fig. 2D) are visible along the longitudinal section, in some cases with pinned walls often hosting bundles of thin helicoidally shaped elements. Some features (vesicular network and long void channels with helicoidal elements), qualitatively similar with those already observed for nut shells and fruit stones [21], suggest a scarcely porous micro-structure enhancing secondary reaction activity [10,24].

The results of the proximate analysis of the stems, summarized in Table 2, testify small differences among samples N.1-5. The volatile matter, VM, fixed carbon, FC, and ash contents approximately vary in the ranges 77–79, 11–14 and 10–12 wt%, respectively. The alkali contents (Table 2) are always very high with values around about 6–10 wt %, with K playing the dominant role, followed by Ca. It is worth noting that these are much higher than those of other food crop residues [37].

3.2. Residue characterization - thermogravimetric and calorimetric parameters

Thermogravimetric curves for the stems of samples N.1-5 are shown in Fig. SM2 of the SM. The parameters, listed in Table 3, include the peak rate of mass loss, $-dY/dt_{peak}$, and corresponding temperature, T_{peak}, the temperature range representative of the conversion interval (the so-called full width at half maximum of the rate curve), fwhm, and the char yield, Y_{773} (the mass fraction for a temperature of 773 K) [41]. Moreover, the volatile mass fraction, released over the temperature interval 550–600 K, where secondary alkali-catalyzed reactions are already active [26,27,43], $Y_{V550\text{-}600}$, and the decomposition temperature, T_{dec}, corresponding to the release of 50 wt% of the total volatile content, are also considered.

The precise chemical composition of potato crop residues is not available but, compared with the typical lignocellulosic biomass, significant contents are reported [36] of starch and proteins, which affect the qualitative and quantitative thermogravimetric behavior [44]. Despite the comparable amounts of charred residues, the T_{dec} (549–567 K) and T_{peak} (554–576 K) temperatures vary by 18 or 22 K, the fwhm range by 37 K and the peak rate by about 33%. Variations are also remarkable (17–28 wt%) on volatile yields released between 550 and 600 K.

This data testifies significant compositional differences among samples N.1-5. In fact, the magnitude of the peak rate increases with the cellulose content. For this specific residue, it may be further enhanced by starch decomposition [44]. Also, higher portions of crystalline cellulose are accompanied by higher characteristic temperatures and narrower fwhm ranges (amorphous structures are predominant for starch [44]). It is known that the cellulose [45] and starch [46] contents increase with plant ageing, with a progressive reduction in the extractives/pectin and protein contents [47]. Kinetic modeling [41], on the other hand, confirms these findings, with volatile product yields from the pseudo-cellulose-starch decomposition increasing from 19 wt% (least aged sample N.3) to 26–27 wt% (most aged samples N.1,2). Hence the contents of the macro-components cellulose and starch, whose volatiles largely contribute to the $Y_{V550\text{-}600}$ and the peak rate values, increase from the sample N.3 to the samples N.4,5 and finally to the samples N.1, 2, in that order. Finally, branches and mainly foliage show [41] lower devolatilization rates.

The measured DSC curves for the samples N.1-5 (potato stems) are reported in Fig. SM3 of the SM. The radiation correction [48–50] is properly considered for the calorimetric curves, using the residue and char specific heats reported in Ref. [51]. For the conditions of the DSC experiments, primary decomposition is the dominant process. In contrast with the results reported for wood, under approximately the same conditions [52], potato stem decomposition is always exothermic. The remarkable rates of char formation, enhanced by alkali catalysis and favored by the high lignin and protein contents, justify these findings. The global heats of primary pyrolysis, evaluated over the temperature range 400–773 K [48] and reported in Table 3, vary from −181 J/g (sample N.3) to −420 J/g (sample N.5). The peak of the heat release rate is reached in correspondence of the third, high-temperature zone of the weight loss curves, representing the decomposition of lignin and protein

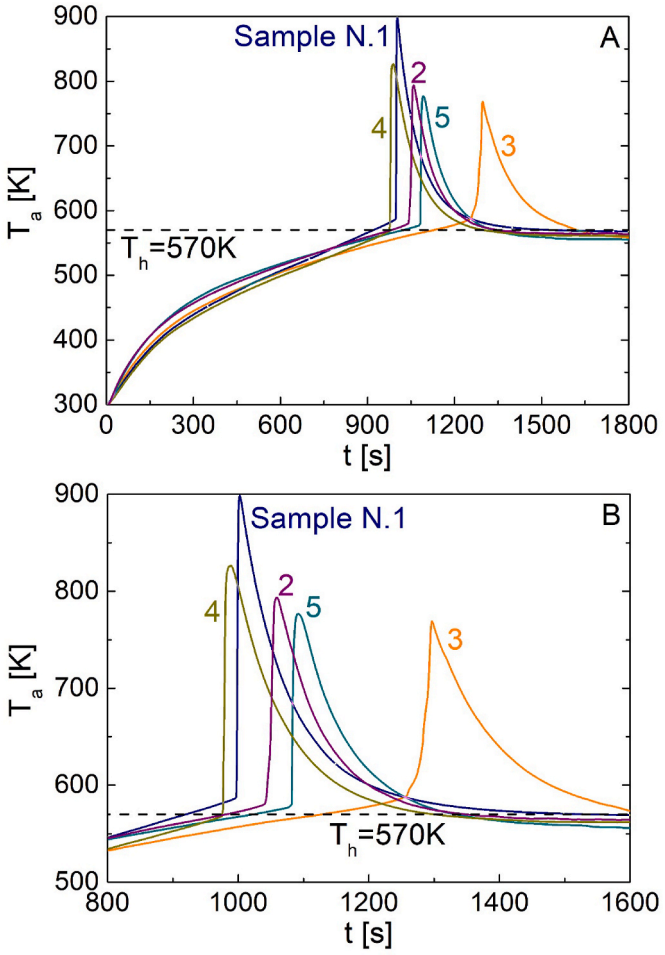

Fig. 3. A-B - Temporal profiles of the spatially averaged temperature of the packed bed during pyrolysis of the potato crop residues, samples N.1-5, (A) and magnified plot of the overheating stage (B) (T_h = 570 K).

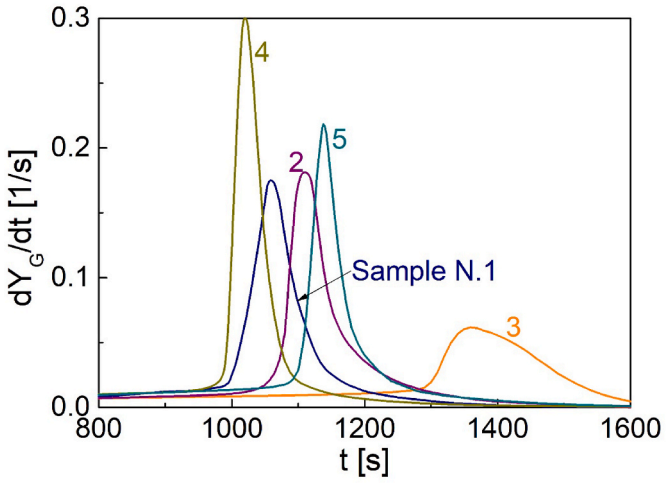

Fig. 4. Temporal profiles of the rate of gas release (the time derivative of the mass fraction of gas released) from the packed bed during pyrolysis the potato crop residues, samples N.1-5, (T_h = 570 K).

which mainly produces char [44]. Overall, the global reaction heats also increase with the importance of the high-temperature zone of primary decomposition.

It is useful to recall that the controlling mechanisms/processes during lignocellulosic biomass pyrolysis mainly depend on the sample properties and operating conditions [53–55]. Thus, for thermogravimetric and calorimetric analysis, small sample mass, slow heating rate and adequate flow conditions generally result into a conversion dominated by the primary reaction rates. These conditions are required not only for the formulation of kinetic mechanisms, to be incorporated in comprehensive transport models, but also for sample characterization (Table 3). Reaction kinetics are never controlling for practical conversion conditions, such as those of the packed-bed reactor of this study. In this case, heat, mass and momentum transfer interact with and primary and secondary reaction activity and related thermicity.

3.3. Effects of feedstock variability on the pyrolytic runaway

The main features of the pyrolytic runaway for the samples N.1-5, for T_h = 570 K, can be seen from the temporal profiles of the spatially averaged temperature, T_a, reported in Fig. 3A-B. In qualitative agreement with previous results [19–21], the packed-bed conversion globally consists of a) pre-heating (or induction), b) pyrolytic runaway, and c) overheating decay. The absence of uniformly distributed and significant porosity in the residue structure (Fig. 2A–D) and the high alkali contents (Table 2) justify the remarkable pyrolysis exothermicity. However, despite the same qualitative trends, the effects of residue variability cause significant quantitative differences. Potassium loading in wood

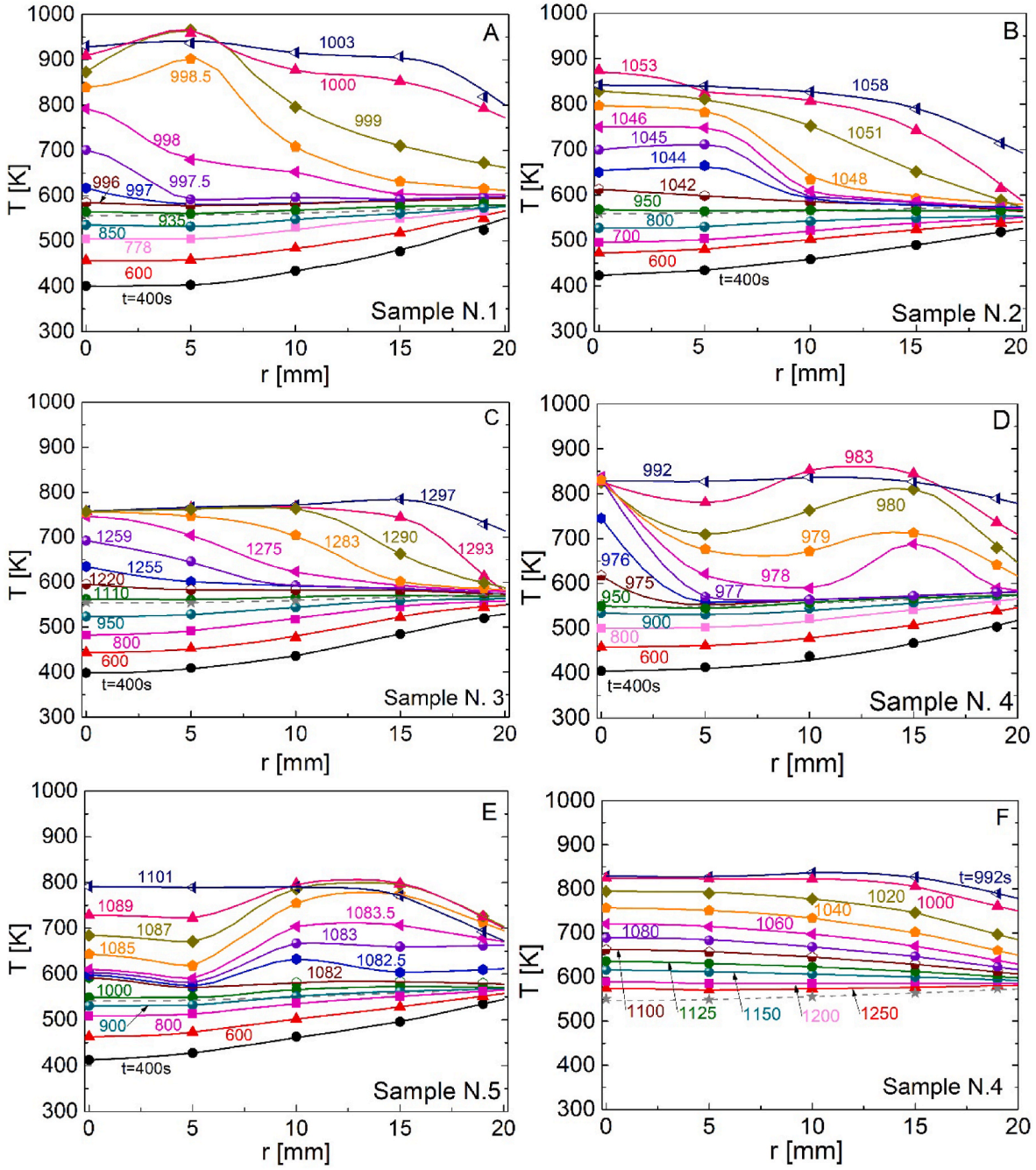

Fig. 5. A–F - Spatial profiles of the packed-bed temperatures for several times for the potato crop residues, samples N.1-5 (A–E), up to the times t_{amax}, and for the decay period for the sample N.4 (F) (T_h = 570 K). The steady profile of the charred bed is indicated with a dashed line.

highly enhances the pyrolysis exothermicity [25–28] but a saturation is reached, in relation to this aspect, for contents above 1.5 wt% [27]. Given the much higher values (5–8.3 wt%, Table 2), the differences in the pyrolytic runaway of samples N.1-5 cannot be ascribed to this property. Instead, as already discussed above, ageing, increasing from the sample N.3 to N.4,5 and N.1,2, is likely to be important.

The gas release rate, dY_G, reported Fig. 4, can be related to the actual conversion rate of the packed bed. In fact, the three lumped classes of products are simultaneously formed, as indicated by the comparable activation energies for their formation rates [55]. Further information on the process dynamics can be obtained from the spatial temperature profiles (Fig. 5A–E) for several times (the temporal profiles at various radial positions are reported in Fig.SM4 of the SM). An example of the overheating decay is shown in Fig. 5F (sample N.4). The spatial temperature profiles at the times of induction and attainment of maximum average temperature are plotted in Fig. 6.

The severity of the pyrolytic runaway can be quantified in terms of overheating with respect to the imposed external heating and conversion rate (characteristic temperatures and times). These can be referred to a local region (actual values) or to the average conditions (spatially averaged values) of the bed. Characteristic parameters, partly already defined [20,21] and graphically represented in Fig. SM5 of the SM (profiles of the average and center bed temperatures, T_a and T_c, are used), are reported in Table 4 and Fig.7A–C, from the least aged to the most aged sample.

They consider the induction time, t_{ind}, identified by a local point/zone of the bed which exhibits a sudden increase in the heating rate, with the corresponding percentage of gas released, Y_{Gind}, and the average temperature, T_{aind}. The pyrolytic runaway is characterized in relation to the time when it begins, t_{pri}, identified in correspondence of a steep variation in the time derivative of the average temperature (a local average heating rate of 2 K/s is used), and the corresponding temperature, T_{apri}, and percentage of gas released, Y_{Gpri}. Other parameters include the maximum average temperature, T_{amax}, and the corresponding time, t_{amax}, the absolute maximum temperature, T_{max}, and the corresponding time, t_{max}, the maximum overshoot of the average temperature, ΔT_{amax}, the maximum local temperature overshoot, ΔT_{max}, and the peak of the gas release rate, dY_{Gpeak}. Moreover, the maximum local bed heating rate, h_b, and the average bed heating rate, h_{ab}, are evaluated. Finally, the overheating decay is identified by a time, t_d, corresponding to a reduction of 90% in the maximum overshoot of the average temperature. In this way, the actual time intervals for pyrolytic runaway, $dt_{pr} = t_{amax}\text{-}t_{pri}$, and overheating, $dt_{overh} = t_d\text{-}t_{pri}$, can be defined. The average temperatures for these time intervals, defined by means of eqn. 1 of the SM, are also considered, T_{apr}, and T_{aoverh}.

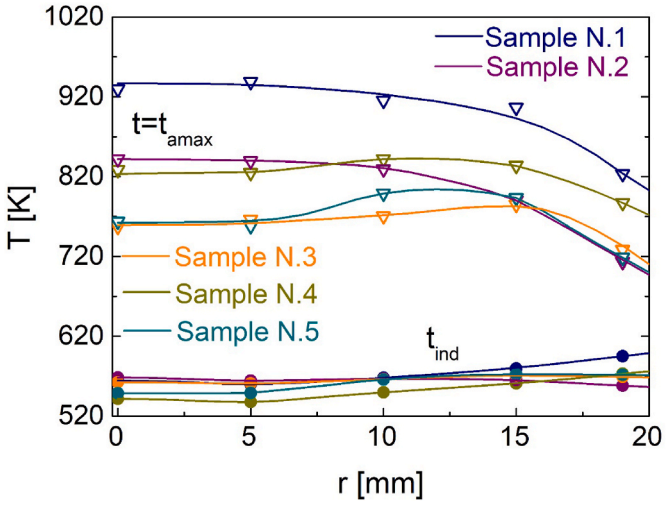

Fig. 6. Spatial profiles of temperature, at the times t_{ind}, and t_{amax}, for the potato crop residues, samples N.1-5 (T_h = 570 K).

Table 4
Pyrolytic runaway parameters for the potato crop residues, samples N.1-5 (the order is from the least to the most aged sample) for a heating temperature, T_h, 570 K): induction time, t_{ind}, with the corresponding spatially averaged temperature of the bed, T_{aind}, and percentage of gas released, Y_{Gind}, time of runaway beginning, t_{pri}, with the corresponding spatially averaged temperature, T_{apri}, and percentage of gas released, Y_{Gpri}, spatially averaged maximum temperature, T_{amax}, with the corresponding time, t_{amax}, and absolute maximum temperature, T_{max}, with the corresponding time, t_{max}, maximum averaged temperature overshoot, ΔT_{amax}, maximum local temperature overshoot, ΔT_{max}, peak of the gas release rate, dY_{Gpeak}, maximum average bed heating rate, h_{ab}, maximum local bed heating rate, h_b, decay time, t_d, and time intervals for pyrolytic runaway, $dt_{pr} = t_{amax}\text{-}t_{pri}$, and overheating, $dt_{overh} = t_d\text{-}t_{pri}$, with the corresponding averaged temperatures, over time and space, T_{apr} and T_{aoverh} (see definitions in Fig. SM4 of the SM and Nomenclature).

	Sample Number				
	3	5	4	2	1
t_{ind} [s]	1110	1000	925	950	935
T_{aind} [K]	568	567	557	564	571
Y_{Gind} [wt%]	24	20.1	10.8	15.3	14.6
t_{pri} [s]	1259	1081.5	975	1042	996
T_{apri} [K]	588	580	568	579	587
Y_{Gpri} [wt%]	33.1	26.7	14.2	20	21.1
t_{amax} [s]	1296	1092	989	1060	1002
T_{amax} [K]	769	777	826	794	898
t_{max} [s]	1296	1092	983	1054	999
T_{max} [K]	785	799	852	874	966
ΔT_{amax} [K]	204	222	265	226	332
ΔT_{max} [K]	218	254	296	314	408
dY_{Gpeak} [1/s]	0.06	0.22	0.3	0.18	0.18
h_{ab} [K/s]	4.3	19.6	18.5	11.3	52
h_b [K/s]	4.7	33	79.6	20.6	155
t_d [s]	1538	1291	1190	1226	1203
dt_{pr} [s]	42	10	14	19	6
T_{apr} [K]	637	739	750	688	771
dt_{overh} [s]	284	209	215	186	206
T_{aoverh} [K]	643	646	671	660	690

Before quantitative comparison of the thermal behavior of the various samples, it is important noticing that the packed-bed experiments show a very good reproducibility. For the characteristic temperatures and related overshoots, minimum and maximum deviations vary between ±0.2 and ± 1.5% and ±1 and ± 2%, respectively. The corresponding figures for the characteristic times are also small (deviation range between ±1 and ± 1.5%). Values are higher but still acceptable for the time intervals of pyrolytic runaway and overheating (deviations between ±5% and ±10%) and maximum heating rates (maxima of ±2% (average) and ±20% (local)).

At the induction time, the thermal conditions of the bed are approximately the same for all the samples. The spatial gradients of temperature are small (Fig.3A–B, 5A-5E and Fig. 6), a feature typical of the pyrolytic runway. The average bed temperatures, T_{aind} (557–571 K) and T_{apri} (568–588 K), are also very close to both the heating temperature (570 K) and the T_{peak} temperatures (555–576 K) (Fig. 7A). The times for the beginning of the conversion, t_{ind} and t_{pri}, show maximum variations of about 100 s, but the sample N.3 whose times are longer and lead to maximum differences around 200–300 s (Table 4) (the higher bulk density may partly be responsible for this result [17]). The average heating rates during bed pre-heating are approximately 0.25–0.3 K/s.

The local maximum temperature overshoot, ΔT_{max}, is exhibited by the sample N.1 (408 K), followed by the samples N.2 (314 K), N. 4 (296 K), N.5 (254 K) and N.3 (218 K) (Table 4, Fig. 7B). As for the average ΔT_{amax} overshoots, the sample N.1 still exhibits the highest value (332 K), but then the sample N.4 (265 K) substitutes the sample N.2 (226 K), in the above order (as discussed below, this can be attributed to different conversion dynamics). The average temperatures during the pyrolytic runaway, T_{apr}, vary in the range 634–771 K, with the limit values

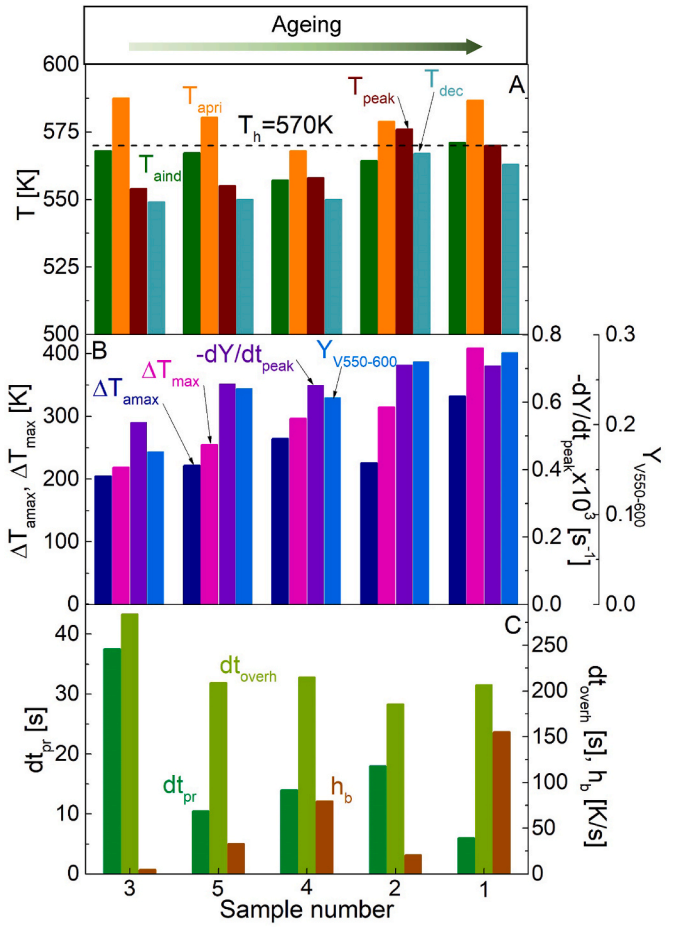

Fig. 7. A–C - Histograms of some characteristic parameters for the samples N.1-5 (T_h = 570 K): T_{aind}, T_{apri}, T_{peak} and T_{dec} (A); ΔT_{amax}, ΔT_{max}, -dY/dt_{peak} and $Y_{V550-600}$ (B); h_b, dt_{pr} and dt_{overh} (C) (the order is from the least to the most aged sample).

corresponding to the samples N.3 and N.1, exceeding the programmed values by about 65–200 K. The average temperature, for the entire overheating period, T_{aoverh}, (643–690 K) deviates by about 70–120 K from the heating temperature.

The overheating period, dt_{overh}, is comparable for the various samples (186–215 s) again apart from the sample N.3 (284 s) (Table 4, Fig. 7C). It is a small fraction (18–23%) of the time for severe pyrolysis to starts, t_{pri}, as always observed for the pyrolytic runaway. Also, the duration of the pyrolytic runaway is very short (about 6–20 s), but the sample N. 3 (about 40 s) (Table 4, Fig. 7C). The maximum local and average heating rates reach 155-5 K/min and 50-4 K/min, respectively, corresponding to the sample N.1 and N.3, respectively.

In summary, the magnitude of the exothermicity display (ΔT_{max}) is maximum and minimum for the samples N.1 and N.3, respectively, representing long- and short-aged plants. Similarly, the samples N.1 and N.3 are characterized by the shortest and longest characteristic times (conversely the fastest and slowest heating rates). Furthermore, the parameters T_{peak} (570–576 K and 554 K) and $Y_{V550-600}$ (27–28 wt% and 17 wt%) are the highest and the lowest for the samples N.1,2 and N.3, respectively (Fig.7A-B) (intermediate values for the samples N.4,5).

The cellulose and starch, whose content increases with plant ageing, play a key role in the global reaction exothermicity. Pyrolysis of biomass and its macro-components becomes successively more exothermic as the pressure is increased, owing to enhanced secondary conversion [49,50]. Modifications are quantitatively stronger for cellulose (and most likely starch, showing a similar pyrolytic behavior [44]), whose vapors exhibit the largest share of sugars [56]. These are responsible for the predominance of exothermic polymerization reactions of the cellulose derived liquids [57]. The higher exothermic formation rates of secondary char favor pyrolytic runway for the most-aged samples (rich in cellulose). Moreover, the average particle size (thickness of the stem walls) also increases with ageing, causing longer intra-particle residence times, further enhancing secondary reaction activity. Hence, the higher amount (and nature) of the organic vapors and the temperature range where they are released, together with prolonged residence times, are plausibly the cause of the higher global exothermicity of the residues with longer average ageing (samples N.1,2, followed by samples N.4,5 and finally N.3). The predominant role of secondary reactions, for the packed-bed conversion, explains the differences of the exothermicity magnitude of the various samples with respect to the results (Table 3) obtained for the conditions of thermal analysis, where only primary decomposition occurs.

Maximum temperatures and temperature overshoots, observed for the sample N.1, are not associated with the maximum rate of gas release (own by the samples N. 4 and 5). This is indeed determined by the bed conversion dynamics (Fig. 5A–E), showing that, for the samples N.1, 2 and 3, a single center-bed trigger point exists, whereas two intra-bed points are evident for the samples N.4 and 5. For the first two samples (induction times of 935 and 950 s, respectively, with the release of 15 wt % of the total gas), the center bed core is promptly pyrolyzed with significant heat transfer towards the colder more external annulus. The external surface of the bed remains at an approximately constant temperature, as long as conversion of the most internal part of the bed takes place. In this way, heat losses from the surface are small, enhancing the overheating magnitude. The dynamics are qualitatively similar for the sample N.3, but the induction time is the longest (1110 s), with a higher amount of gas produced (24 wt%) and a slower average conversion rate (Fig. 4).

For the samples N.4 and 5, center-bed trigger points appear (at 925 and 1000 s with amounts of released gas equal to 11 and 20 wt%, respectively). Furthermore, shortly after another trigger point clearly appears (at 978 and 1082.5 s and r = 15 and 10 mm, respectively). The presence of multiple trigger points causes that different bed zones are simultaneously pyrolyzed, justifying the highest rates of gas (and volatile) release (Fig. 4). These are associated with reduced intra-bed residence time of volatile products. For the sample N.5, the conversion of the central bed core is slower than that of the external annulus, quantitatively more important, where the second trigger zone is observed. The position of this nearby the external surface and the longer dynamics cause higher heat losses, and thus reduced overheating. In this regard, small differences in the residue properties with respect to sample N. 4 (i. e. stem thickness, potassium contents, chemical composition) may also play a role.

Previous results for the sample N.2 [20] report a shift from a single center-bed to multiple intra-bed trigger points for the pyrolytic runaway, as the external heating conditions become slightly more severe (heating temperatures in the range 570–590 K). The two trigger modalities are related to activation temperatures (e. g. T_{peak}) for the pyrolysis reactions approximately coincident or slightly lower than the heating temperature, T_h, as it is the case (Fig. 7A) for the samples N.1–2 and N.4-5, respectively. More severe external heating leads to a trigger zone nearby the lateral bed surface [20]. Again, the very slow primary decomposition rates and the nature of primary vapors may be responsible for the behavior of the sample N.3 (a single center-bed trigger point despite activation temperatures lower than T_h) not in line with the previous observation. Detailed mathematical modeling could be useful to clarify these aspects of pyrolytic runaway.

3.4. Pyrolysis products

The yields of the three lumped product classes and the gaseous species are listed in Table 5 for the samples N.1-5. As already observed, the temperature overshoots are remarkable but the average

Table 5
Yields of char, liquids, gas, and gas components, expressed as percent of the initial dry mass, for the packed-bed pyrolysis of the potato crop residues, samples N.1-5 (heating temperature, T_h, 570 K).

Sample Number	Char [wt%]	Liquids [wt%]	Gas [wt%]	CO_2 [wt%]	CO [wt%]	CH_4 [wt%]
1	40.4	37.1	19.6	13.4	5.4	0.6
2	40.4	35.9	20.7	16.4	3.3	0.6
3	43.2	37.9	16.9	14.1	2.4	0.2
4	42.4	34.3	21.1	15.9	4.1	0.6
5	41.6	34.5	21.9	16.1	4.9	0.5

temperatures during overheating vary in a narrow range (643–690 K) and, apart from the sample N.3 (284 s) the duration is almost the same (around 186–215 s). This may, in part, justify the small differences in the yields of the lumped product classes. Indeed, the total yields of char and gas vary between 60 and 63 wt%. Given mass closures around 96–97 wt %, the liquid yields, also including water, are also approximately the same for the various samples (34–38 wt%).

It can be noticed that the char yields are barely higher for the sample N.3, in agreement with the results of thermogravimetric analysis, possibly resulting from the intrinsic sample properties. However, it is not possible to distinguish primary and secondary contributions.

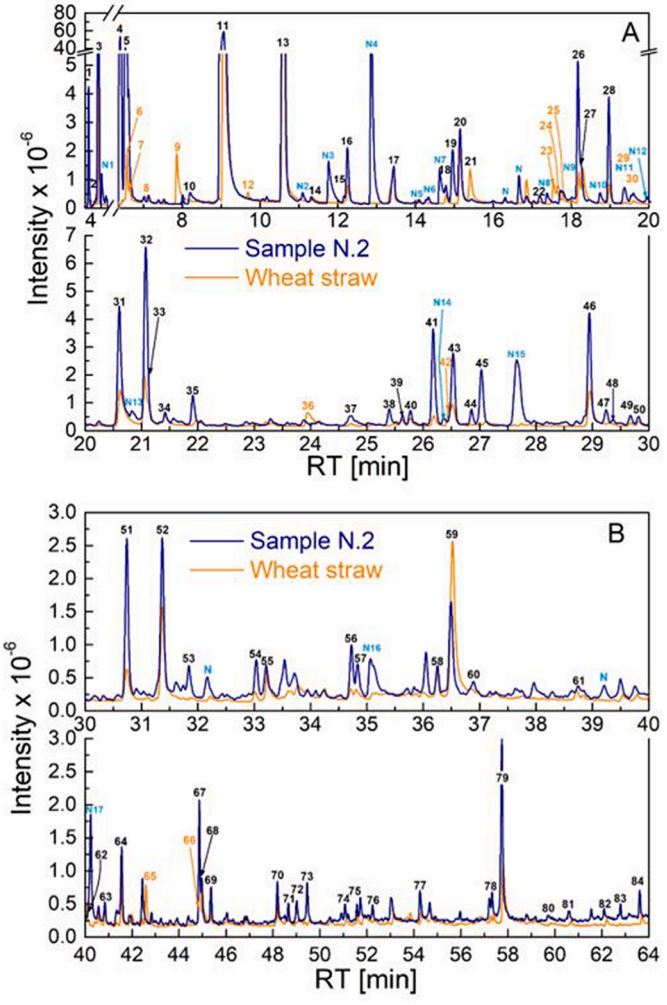

Fig. 8. A–B - Total ion chromatogram (TIC) registered for the liquids (water and organic fraction) produced from potato crop residues, sample N.2, (T_h = 570 K) and wheat straw pyrolysis (T_h = 725 K [40]) (the peak number corresponds to the species listed in Table 6).

Table 6
Pyrolysis liquid compounds of the potato crop residue (sample N.2, T_h = 570 K) and wheat straw [40] (T_h = 725 K) identified by GC/MS with retention times (RT) reported in Fig. 9A–B (the identification of the peaks is based on computer matching of the mass spectra with the NIST library, match %, or on the retention times of known species injected in the chromatographic column, i).

N.	Compound	RT [min]	Match [%]
1	Oxygen	3.88	99.9
2	Acetaldehyde	4.25	91.7
N1	Trimethylamine	4.52	91.4
3	Methyl alcohol	4.38	94.7
4	Ethylacetate	6.31	92.4
5	Tetrahydrofuran	6.44	92.7
6	2,3-Butanedione	6.58	96.8
7	2-Butanone	6.68	87.6
8	3-Pentanone	7.05	83.1
9	Hydroxyacetaldehyde	7.87	i
10	Formic acid	8.11	i
11	Acetic acid	9.11	i
12	2,3-Pentanedione	9.69	85.2
13	Hydroxypropanone	10.62	i
N2	Pyrazine	10.87	90.7
14	Acetic acid,hydroxy-,methylester	11.35	87.3
N3	Pyridine	11.49	94.6
15	3-Penten-2-one	12.21	91
16	2-Hydroxy-3-butanone	12.27	97.0
N4	2,4-Dimethyl-2-oxazoline-4-methanol	12.86	78.5
17	Propanoic acid	13.40	i
N5	*Unknown nitrogenous specie*	14.21	
N6	*Unknown nitrogenous specie*	14.27	
N7	2-Methylpyridine	14.55	91.8
18	Cyclopentanone	14.77	87.9
19	1,2-Ethanediol	14.90	84.9
20	1-Hydroxy-2-butanone	15.14	i
21	1,2-Ethanediol,monoacetate	15.39	80.0
22	2-Methylpropanoic acid anhydride	16.94	91.4
N8	2,6-Dimethylpyridine	14.55	91.8
23	Butanedial	17.52	91.4
24	Propanoic acid,2-oxo,methylestere	17.64	82.3
N9	3- Methylpyridine	17.62	88.7
25	Butanoic acid	17.78	79.6
26	2-Cyclopentenone	18.18	90.3
27	Furfural	18.30	i
N10	2-Ethylpyridine	18.79	83.0
28	4-Hydroxy-4-methylpentanone	18.97	87.9
29	3-Methyl-2-cyclopentenone	19.40	
N11	4,6-Dimethylpyridine	19.40	78.9
30	1-Hydroxy-2-pentanone	19.60	86.5
N12	2,3-Dimethylpyrazine	19.97	82.0
31	Furfurylalcohol	20.63	i
N13	2,4-Dimethylpyridine	20.89	88.3
32	Acetoxyacetone	21.04	i
33	2-Methyl-2-cyclopentenone	21.12	i
34	2-Butanone	21.46	88.3
35	Acetylfuran	21.96	I
36	2-Hydroxy-2-cyclopenten-1-one	23.92	97.0
37	2,5-Hexanedione	24.70	81
38	5-Methyl-2-furaldehyde	25.42	I
39	Propanoic acid, ethylester	25.60	83.5
40	1-Hydroxy-2-butanone acetate	25.77	89.8
41	3-Methyl-2-cyclopentenone	26.18	I
N14	3-Methoxypyridine	26.30	83.5
42	2-Propyltetrahydrofuran	26.43	85.0
43	Butyrolactone	26.52	95.0
44	3,4-Dimethyl-2-cyclopenten-1-one	26.85	85.4
45	2(5H)-Furanone	27.10	I
N15	3,4-Dimethyl-2-oxozolinep-4-methanol	27.65	90.5
46	2-Hydroxy-1-methylcyclopenten-3-one	28.96	95.6
47	2(5H)-Furanone,-3-methyl-	29.27	82.3
48	2,3,4-Trimethyl-2-cyclopenten-1-one	29.36	81.4
49	2,4-Dimethyl-1,3-cyclopentanedione	29.66	74.5
50	2-Furanone,2,5-dihydro-3,5-dimethyl	29.82	88.1
51	Phenol	30.74	I
52	Guaiacol	31.36	I
53	3-Ethyl-2-cyclopenten-1-one	31.85	87.6
54	o-Cresol	33.10	I
55	3-Ethyl-2-hydroxy-2-cyclopenten-1-one	33.24	I

(*continued on next page*)

Table 6 (*continued*)

N.	Compound	RT [min]	Match [%]
56	p-Cresol	34.71	I
57	m-Cresol	34.81	I
N16	2-Pyrroldione	35.10	86.2
58	4-Methylguaiacol	36.23	I
59	Pentanal	36.52	75.5
60	2,4-Dimethylphenol	36.85	I
61	2-Ethylphenol	38.73	I
62	4-Ethylguaiacol	40.03	90.7
N17	3-Hydroxypyridine	27.65	90.6
63	*Unknown sugar*	40.86	–
64	1,4:3,6-Dianhydro-#x03B1;-d-glucopyranose	41.55	91.1
65	4-Vinylguaiacol	42.59	84.8
66	1,2-Benzenediol	44.74	87.2
67	Syringol	44.87	I
68	5-Hydroxymethyldihydrofuran-2-one	44.98	87.0
69	*Unknown sugar*		
70	*Unknown sugar*		
71	1,2,3-Trimethoxybenzene	48.65	79
72	Vanillin	49.16	I
73	Hydroquinone	49.41	I
74	Methylhydroquinone	51.07	85.6
75	1,2,3-Trimethoxy-5-methylbenzene	51.62	78.6
76	Acetoguaiacone	52.35	I
77	Guaiacylacetone	54.34	I
78	*Unknown sugar*	57.42	–
79	Levoglucosan	57.86	I
80	Syringaldehyde	59.80	I
81	*Unknown sugar*	60.66	–
82	Acetosyringone	62.21	88.7
83	Diisobutylphthalate	62.87	85.8
84	Butyrophenone-2,4,6-trihyroxy-3-methyl	63.69	86.0

Moreover, the yields of CO are the highest and the lowest for the samples N.1 and N.3, respectively. This is most likely a consequence of a different activity of secondary reactions which, in turn, affects the global thermicity of the process. Percentage variations on the CO_2 yields are smaller, testifying that this is mainly generated from primary decomposition.

The chemical characterization of the liquid product has been carried out for the samples N.2 and N.3, representing, on average, the behavior of the long- and short-aged residues, aimed in the first place at ascertaining the possible presence of compounds other than those typically observed for lignocellulosic biomass [58]. For this reason, pyrolysis liquids obtained from the sample N.2 and wheat straw (heating temperature of 725 K and absence of pyrolytic runaway with a maximum temperature overshoot of 44 K [40]) are compared in Fig.8A-B and Table 6.

The differences between the two liquid products are expected to be caused, in the first place, by the chemical composition. The contents of extractives, pectin, starch and protein are negligible for wheat straw and remarkable for potato crop residues. The amounts of alkali compounds are also different (much higher for potato crop residues). In the second place, a highly different activity of secondary reactions is plausible, caused by different microstructures and particle sizes between the two feedstocks.

Indigenous or added alkali compounds in lignocellulosic materials modify primary decomposition reactions of biomass macro-components and favor secondary reaction activity. The formation of char, water and gases is augmented at the expense of organic condensable products [25–28]. Both the depolymerization path (formation of levoglucosan, anhydro-sugars, and higher oligomers) and the competitive decarbonylating and fragmentation reactions (formation of hydroxy-acetaldehyde, formaldehyde, acetol, and methylglyoxal) are progressively inhibited.

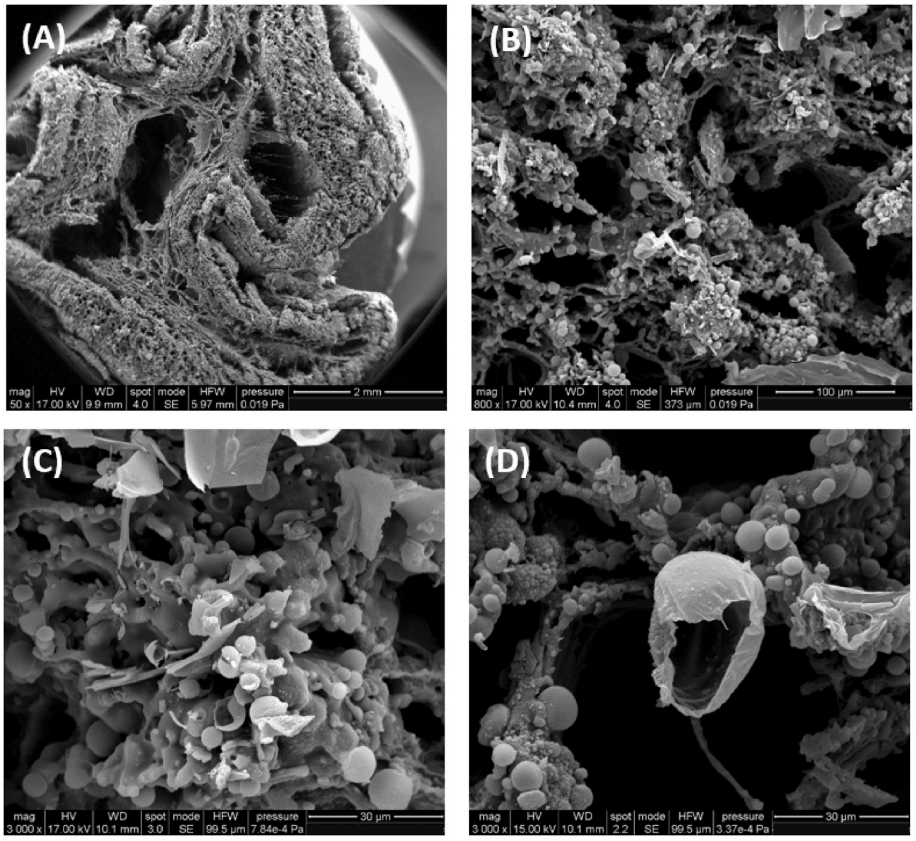

Fig. 9. A–D - SEM images of chars from packed-bed pyrolysis of potato crop residues (sample N.1, T_h = 570 K): stem cross section (A) and magnified views of the morphological structure (B–D).

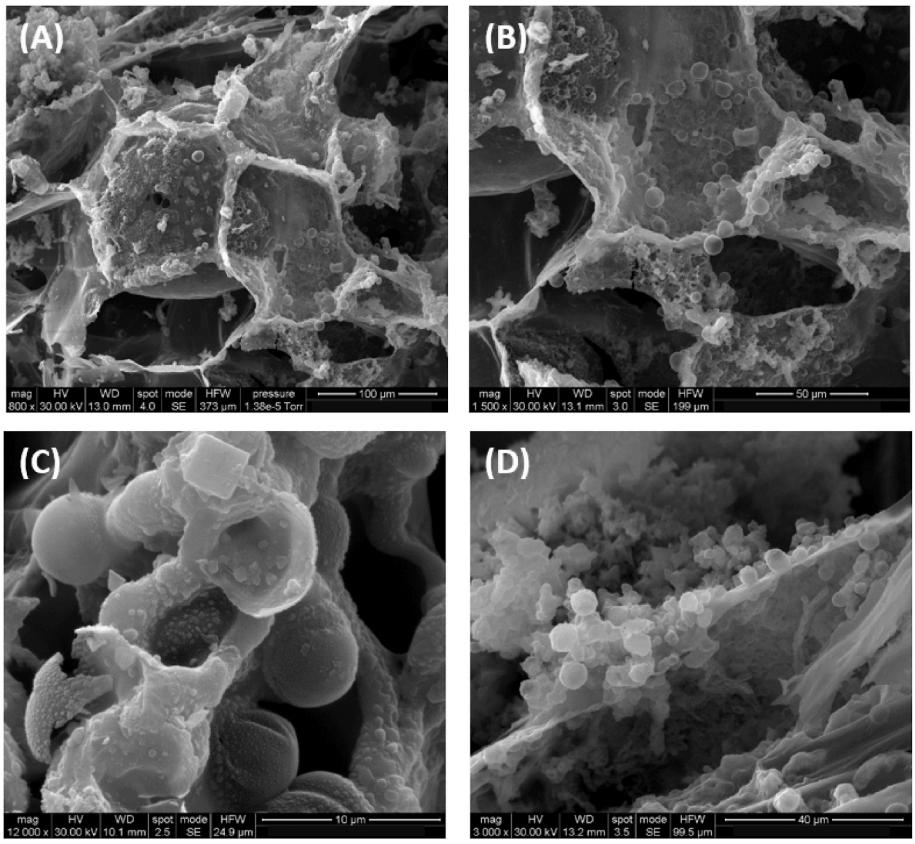

Fig. 10. A–D - SEM images of chars from packed-bed pyrolysis of potato crop residues (sample N.1, $T_h = 570$ K): magnified views of the morphological structure with deposits across (A–C) and along (D) the stem.

Instead, the production of some minor carbohydrates, including cyclopentenones, furans and phenols is significantly enhanced [59,60]. Primary anhydro-sugars and levoglucosan are also the precursors of secondary processes giving char through re-arrangement, polymerization and crosslinking reactions [28], all affected by the interactions with alkali metals. Consequently, some compounds (peaks 6–9, 12, 23, 24, 36, 42, 65, 66 and 67 of Fig. 9A-B) observed for wheat straw are not detected for the potato crop residue, in particular hydroxy-acetaldehyde (peak 9), one of chief components of wood fast pyrolysis oil [58]. Again, as expected from alkali catalysis and based on the chromatogram peak heights, higher yields are obtained for some furans (peaks 31, 35, 38, 43, 45, 47), cyclopentenones (41, 46, 44, 48) and phenols (peaks 51–54, 56–58, 67, 72, 73). The last compound group is originated from the decomposition of lignin [44,58] and proteins [44]. Moreover, for the potato crop residue, the latter is the origin [44] of several nitrogenous compounds, including some pyridines, (peaks N1–N17 of Fig. 8A-B). The yield of levoglucosan (peak 79) is higher than that generated from wheat straw. Finally, two unknown sugars (peaks 69, 70) are also identified. Although the formation of sugars from cellulose is completely hindered in the presence of alkali compounds, the decomposition of starch, again not contributing to the chemical composition of wheat straw, might be responsible for the results observed. Overall, the compounds of the potato crop residue liquid are the same as for the pyrolysis of biomass materials catalyzed by alkali compounds, considering the contributions of starch and proteins in the feedstock chemical composition.

A comparison between the chromatograms of the samples N.2 and N.3 is made in Fig.SM6 of the SM. There are no qualitative differences in the slate of products. Quantitative differences, based on the peak heights, are also negligible but a few species. The yields of levoglucosan (peak 79), formic acid (peak 10), 5-methyl-2-furaldehyde (peak 38) and pentanal (peak 59) are significantly lower for the sample N.3. On the contrary, some minor carbohydrates (peaks 17, 20 and 28) and furans (peaks 31, 43 and 68) are present in higher amounts. This confirms the lower contents of cellulose/starch and the higher contents of low-temperature compounds for the short-aged sample N.3, as indicated by the thermogravimetric analysis.

3.5. *Morphological structure of char*

The morphological structure of the chars generated from the packed-bed pyrolysis can be observed in Fig. 9A–D and Fig. 10A–D for the sample N.1 (the same qualitative behavior is observed in all cases). At a first glance, it appears that the main features of the potato stem are preserved (Fig. 9A). However, the magnified images (Fig. 9B–D) show that the walls of the cellular structure are fully covered by bubbles of variable size, which are generally intact or, in a few cases, burst. Bubbles are also observed over the entire surface of the closed alveola (Fig. 10A-B). Small deposits rather regularly shaped are randomly scattered over the char surfaces, including those of the bubbles (Fig. 10C). Moreover, mainly along the longitudinal direction of the charred stem, they often are heaped up (Fig. 10D).

The EDX analysis confirms that bubbles are essentially made by organic matter (contents of C and O in the range 65–75 wt% and 10–20 wt%, respectively, with contributions from K (9–15 wt%) and Cl (2–5 wt %)). Instead, the randomly scattered or heaped up deposits appear to mainly consist of inorganic matter, with large contributions from K (25–45 wt%), Ca (5–30 wt%), Cl (2–5 wt%) and Mg (0.5–1 wt%), as expected from the previously described ICP-MS results (Table 2). Chlorine, most likely originally present in the form of water-soluble chlorides, is only partly released during pyrolysis [61], owing to the

moderate maximum temperatures.

It is understandable that, in consequence of the very fast heat release rates that are locally caused by the strong pyrolysis exothermicity, the particles undergo a molten phase. Hence, for getting out, the vapors and gases cause swelling and bubble formation (fractures are not observed). The scarce micro-porosity combined with remarkable particle thicknesses indicate significant activity of secondary reactions. Fusion phenomena are observed everywhere for the different parts of the feed, given diffused overheating across the particles. In other words, for mild external heating and absence of control, packed-bed conversion occurs under the conditions of intrinsically driven fast pyrolysis. These are established without the need to use special reactor configurations, i. e. ablative reactors or lean-phase reactors with small-sized feed [2], to overcome the well-known limitations in the external heat transfer rates. Another specification concerns the presence of very large amounts of indigenous alkali metals so, to be more precise, the pyrolytic runway of potato crop residues is, in a practical way, an intrinsically fast pyrolysis process, in-situ catalyzed by alkali metals.

4. Conclusions

Packed bed pyrolysis of potato crop residues, exposed to very mild radiative heating, takes place under a pyrolytic runaway regime. The very high contents of alkali metals, which catalyze both primary and secondary charring, and the long intra-particle residence time of primary vapors, caused by a cellular structure with low porosity, are the main factors responsible for the high global exothermicity of the conversion. The conversion process can be considered as an in-situ catalytic and intrinsically fast pyrolysis, with thermal conditions highly different from those of external heating. Despite the qualitatively similar dynamics, quantitative differences introduced by feedstock variability are significant.

Maximum temperature overshoots, with respect to the heating conditions, vary approximately in the range 410–220 K (local values) and 330-200 K (average bed values). The duration of the pyrolytic runaway, from the beginning to the overheating climax, varies in the range 6–42 s, which is always a small fraction of the induction time (about 0.6–4%). Feedstock variability essentially corresponds to variable average ageing of the plants. For successively longer ageing, the characteristic particle size increases. The cellulose and starch contents also increase. The larger amounts and the higher reactivity of primary vapors produced by these macro-components, as well as the prolonged intra-particle residence, justify the higher thermal severity of the pyrolytic runaway observed for longer-aged samples. Hence, the feedstock chemical composition and the timing of reactive vapor release are important factors for the magnitude of the pyrolysis exothermicity display.

The lumped classes of products show yields varying in a narrow range and exhibit comparable properties. Char is the most important product, amounting to about 40–43 wt%. Most likely owing to the always rather fast heating, surfaces show extensive melting and scattered alkali deposits. The total liquid product, amounting to about 34–38 wt %, presents interesting quantities of cyclopentenones, furans and phenols, which can find useful applications in various industrial sectors, and nitrogenous compounds originated from protein decomposition.

Further investigation is needed about the pyrolytic runaway of agricultural residues with special emphasis on feedstock screening, pretreatments, application of modulated profiles of heat inputs (instead of the usual constant setpoint), co-feeding materials with highly different thermicity and process modeling.

Credit author statement

Carmen Branca: Conceptualization, Methodology, Investigation, Data curation, Writing- Original draft preparation, Reviewing and Editing, Antonio Galgano: Conceptualization, Methodology, Investigation, Data curation, Writing- Original draft preparation, Reviewing and Editing, Colomba Di Blasi: Conceptualization, Methodology, Investigation, Data curation, Writing- Original draft preparation, Reviewing and Editing.

Declaration of competing interest

The authors declare that they have no known competing financial interests or personal relationships that could have appeared to influence the work reported in this paper.

Data availability

The authors do not have permission to share data.

Acknowledgments

The authors thank Mr. Luciano Cortese (Istituto di Scienze e Tecnologie per l'Energia e la Mobilità Sostenibili, CNR, Napoli, Italy) for the SEM images of the residues and the chars, and Mr. Fernando Stanzione (Istituto di Scienze e Tecnologie per l'Energia e la Mobilità Sostenibili, CNR, Napoli, Italy) for the ICP-MS analysis of the ashes.

Appendix A. Supplementary data

Supplementary data to this article can be found online at https://doi.org/10.1016/j.energy.2023.127507.

References

[1] Huang Y, Li B, Liu D, Xie X, Zhang H, Sun H, Hu X, Zhang S. Fundamental advances in biomass autothermal/oxidative pyrolysis: a review. ACS Sustainable Chem Eng 2020;8:11888–905.
[2] Vamvuka D. Bio-oil, solid and gaseous biofuels from biomass pyrolysis processes—an overview. Int J Energy Res 2011;35:835–62.
[3] Gomez-Barea A, Leckner B. Modeling of biomass gasification in fluidized bed. Prog Energy Combust Sci 2010;36:444–509.
[4] Crombie K, Mašek O. Investigating the potential for a self-sustaining slow pyrolysis system under varying operating conditions. Biores. Technol. 2014;162:148–56.
[5] Abrego J, Plaza D, Luno F, María Atienza-Martínez M, Gea G. Pyrolysis of cashew nutshells: characterization of products and energy balance. Energy 2018;158:72–80.
[6] Amutio M, Lopez G, Aguado R, Bilbao J, Olazar M. Biomass oxidative flash pyrolysis: autothermal operation, yields and product properties. Energy Fuel 2012;26:1353–62.
[7] Phama XH, Piriou B, Salvador S, Valette J, Van de Steene L. Oxidative pyrolysis of pine wood, wheat straw and miscanthus pellets in a fixed bed. Fuel Process Technol 2018;178:226–35.
[8] Polin JP, Peterson CA, Whitmer LE, Smith RG, Brown RC. Process intensification of biomass fast pyrolysis through autothermal operation of a fluidized bed reactor. Appl Energy 2019;249:276–85.
[9] Mendoza-Martinez C, Sermyagina E, Saari J, Faria Ramos V, Vakkilainen E, Cardoso M, Alves Rocha EP. Fast oxidative pyrolysis of eucalyptus wood residues to replace fossil oil in pulp industry. Energy 2023;263:126076.
[10] Di Blasi C, Branca C, Galgano A. On the experimental evidence of exothermicity in wood and biomass pyrolysis. Energy Technol 2017;5:19–29.
[11] Di Blasi C, Branca C, Santoro A, Perez Bermudez RA. Weight loss dynamics of wood chips under fast radiative heating. J Anal Appl Pyrolysis 2001;57:77–90.
[12] Becidan M, Skreiberg O, Hustad JE. Products distribution and gas release in pyrolysis of thermally thick biomass residues samples. J Anal Appl Pyrolysis 2007;78:207–13.
[13] Manya JJ, Ruiz J, Arauzo J. Some peculiarities of conventional pyrolysis of several agricultural residues in a packed bed reactor. Ind Eng Chem Res 2007;46:9061–70.
[14] Park WC, Atreya A, Baum HR. Experimental and theoretical investigation of heat and mass transfer processes during wood pyrolysis. Combust Flame 2010;157:481–94.
[15] Rousset P, Davrieux F, Macedo L, Perré P. Characterisation of the torrefaction of beech wood using NIRS: combined effects of temperature and duration. Biomass Bioenergy 2011;35:1219–26.
[16] Di Blasi C, Branca C, Masotta F, De Biase E. Experimental analysis of reaction heat effects during beech wood pyrolysis. Energy Fuel 2013;27:2665–74.
[17] Di Blasi C, Branca C, Lombardi V, Ciappa P, Di Giacomo C. Effects of particle size and density on the packed-bed pyrolysis of wood. Energy Fuel 2013;27:6781–91.
[18] Zobel N, Anca-Couce A. Influence of intraparticle secondary heterogeneous reactions on the reaction enthalpy of wood pyrolysis. J Anal Appl Pyrolysis 2015;116:281–6.
[19] Di Blasi C, Branca C, Sarnataro FE, Gallo A. Thermal runaway in the pyrolysis of some lignocellulosic biomasses. Energy Fuel 2014;28:2684–96.

[20] Di Blasi C, Branca C, Galgano A, Autiero G. Analysis of the pyrolytic runaway dynamics during agricultural waste conversion. Energy Fuel 2018;32:9530–40.
[21] Di Blasi C, Galgano A, Branca C. Exothermic events of nut shell and fruit stone pyrolysis. ACS Sustainable Chem Eng 2019;7:9035–49.
[22] Branca C, Di Blasi C, Galgano A. Chemical characterization of volatile products of biomass pyrolysis under significant reaction-induced overheating. J Anal Appl Pyrolysis 2016;19:8–17.
[23] Abrego J, Atienza-Martínez M, Plou F, Arauzo J. Heat requirement for fixed bed pyrolysis of beechwood chips. Energy 2019;178:145–57.
[24] Anca-Couce A. Reaction mechanisms and multi-scale modelling of lignocellulosic biomass pyrolysis. Prog Energy Combust Sci 2016;53:41–79.
[25] Shah MH, Deng L, Bennadji HH, Fisher EM. Pyrolysis of potassium-doped wood at the centimeter and submillimeter scales. Energy Fuel 2015;29:7350–7.
[26] Di Blasi C, Branca C, Galgano A. Influences of potassium hydroxide on the rate and thermicity of wood pyrolysis reactions. Energy Fuel 2017;31:6154–62.
[27] Di Blasi C, Branca C, Galgano A. Role of the potassium chemical state in the global exothermicity of wood packed-bed pyrolysis. Ind Eng Chem Res 2018;57:11561–71.
[28] Nzihou A, Stanmore B, Lyczko N, Pham Minh D. The catalytic effect of inherent and adsorbed metals on the fast/flash pyrolysis of biomass: a review. Energy 2019;170:326–37.
[29] Di Blasi C, Branca C, Galgano A. Flame retarding of wood by impregnation with boric acid - pyrolysis products and char oxidation rates. Polym Degrad Stabil 2007;92:752–64.
[30] Di Blasi C, Branca C, Galgano A, D'Agostino P. Thermal behavior of beech wood during sulfuric acid catalyzed pyrolysis. Energy Fuel 2015;29:6476–84.
[31] Di Blasi C, Branca C, Galgano A, Zenone F. Modifications in the thermicity of the pyrolysis reactions of $ZnCl_2$-loaded wood. Ind Eng Chem Res 2015;54:12741–9.
[32] Di Blasi C, Branca C, Galgano A, Gallo B. Role of pretreatments in the thermal runaway of hazelnut shell pyrolysis. Energy Fuel 2015;29:2514–26.
[33] Branca C, Di Blasi C, Galgano A, Clemente M. Analysis of the interactions between moisture evaporation and exothermic pyrolysis of hazelnut shells. Energy Fuel 2016;30:7878–86.
[34] Soltanieh A, Jazini M, Karimi K. Biorefinery for efficient xanthan gum, ethanol, and biogas production from potato crop residues. Biomass Bioenergy 2022;158:106354.
[35] Devaux A, Goffart JP, Kromann P, Andrade-Piedra J, Polar V, Hareau G. The potato of the future: opportunities and challenges in sustainable agri-food systems. Potato Res 2021;64:681–720.
[36] Kolbe H, Stephan-Beckmann S. Development, growth and chemical composition of the potato crop (Solanum tuberosum L.). Potato Res 1997;40:111–29.
[37] Vassilev SV, Baxter B, Andersen LK, Vassileva CG. An overview of the chemical composition of biomass. Fuel 2010;89:913–33.
[38] Rego F, Soares Dias AP, Casquilho M, Rosa FC, Rodrigues A. Pyrolysis kinetics of short rotation coppice poplar biomass. Energy 2020;207:11891.
[39] Ray AE, Williams CL, Hoover AN, Li C, Sale KL, Emerson RM, Klinger J, Oksen E, Narani A, Yan J, Beavers CM, Tanjore D, Yunes M, Bose E, Leal JH, Bowen JL, Wolfrum EJ, Resch MG, Semelsberger TA, Donohoe BS. Multiscale characterization of lignocellulosic biomass variability and its implications to preprocessing and conversion: a case study for corn stover. ACS Sustainable Chem Eng 2020;8:3218–30.
[40] Branca C, Di Blasi C, Galgano A. Pyrolytic conversion of wastes from cereal, protein and oil-protein crops. J Anal Appl Pyrolysis 2017;127:426–35.
[41] Branca C, Di Blasi C. Modeling the effects of cultivar and harvest on the decomposition kinetics of potato crop residues. Fuel 2023;339:127419.
[42] Branca C, Di Blasi C, Galgano A. Catalyst screening for the production of furfural from corncob pyrolysis. Energy Fuel 2012;26:1520–30.
[43] Hu M, Ye Z, Zhang Q, Xue Q, Li Z, Wang J, Pan Z. Towards understanding the chemical reactions between KOH and oxygen-containing groups during KOH-catalyzed pyrolysis of biomass. Energy 2022;245:123286.
[44] Zong P, Jiang Y, Tian Y, Li J, Yuan M, Ji Y, Chen M, Li D, Qiao Y. Pyrolysis behavior and product distributions of biomass six group components: starch, cellulose, hemicellulose, lignin, protein and oil. Energy Convers Manag 2020;216:112777.
[45] Lee CM, Kafle K, Belias DW, Park YB, Glick RE, Haigler CH, Kim SH. Comprehensive analysis of cellulose content, crystallinity, and lateral packing in Gossypium hirsutum and Gossypium barbadense cotton fibers using sum frequency generation, infrared and Raman spectroscopy, and X-ray diffraction. Cellulose 2015;22:971–89.
[46] McKinley BA, Casto AL, Rooney WL, Mullet JE. Developmental dynamics of stem starch accumulation in Sorghum bicolor. Plant Direct 2018;2:1–15.
[47] Pordesimo LO, Hames BR, Sokhansanj S, Edens WC. Variation in corn stover composition and energy content with crop maturity. Biomass Bioenergy 2005;28:366–74.
[48] Rath J, Wolfinger MG, Steiner G, Krammer G, Barontini F, Cozzani V. Heat of wood pyrolysis. Fuel 2003;82:81–91.
[49] Basile L, Tugnoli A, Stramigioli C, Cozzani V. Influence of pressure on the heat of biomass pyrolysis. Fuel 2014;137:277–84.
[50] Basile L, Tugnoli A, Cozzani V. Influence of macrocomponents on the pyrolysis heat demand of lignocellulosic biomass. Ind Eng Chem Res 2017;56:6432–40.
[51] Chen Q, Yang R, Zhao B, Li Y, Wang S, Wu H, Zhuo Y, Chen C. Investigation of heat of biomass pyrolysis and secondary reactions by simultaneous thermogravimetry and differential scanning calorimetry. Fuel 2014;134:467–76.
[52] Branca C, Di Blasi C. A summative model for the pyrolysis reaction heats of beech wood. Thermochim Acta 2016;638:10–6.
[53] Di Blasi C. Kinetic and heat transfer control in the slow and flash pyrolysis of solids. Ind Eng Chem Res 1996;35:37–47.
[54] Di Blasi C. Influences of model assumptions on the predictions of cellulose pyrolysis in the heat transfer-controlled regime. Fuel 1996;75:58–66.
[55] Di Blasi C. Modeling chemical and physical processes of wood and biomass pyrolysis. Prog Energy Combust Sci 2008;34:47–90.
[56] Carrier M, Windt M, Ziegler B, Appelt J, Saake B, Meier D, Bridgwater A. Quantitative insights into the fast pyrolysis of extracted cellulose, hemicelluloses, and lignin. ChemSusChem 2017;10:3212–24.
[57] Branca C, Di Blasi C, Elefante R. Devolatilization of conventional pyrolysis oils generated from biomass and cellulose. Energy Fuel 2006;20:2253–61.
[58] Auersvald M, Macek T, Schulzke T, Staš M, Šimáček P. Influence of biomass type on the composition of bio-oils from ablative fast pyrolysis. J Anal Appl Pyrolysis 2020;150:104838.
[59] Di Blasi C, Galgano A, Branca C. Effects of potassium hydroxide impregnation on wood pyrolysis. Energy Fuel 2009;23:1045–54.
[60] Di Blasi C C, Galgano A A, Branca C C. Influences of the chemical state of alkaline compounds and the nature of alkali metal on wood pyrolysis. Ind Eng Chem Res 2009;48:3359–69.
[61] Du S, Wang X, Shao J, Yang H, Xu G, Chen H. Releasing behavior of chlorine and fluorine during agricultural waste pyrolysis. Energy 2014;74:295–300.